Experimental and Theoretical Studies of the Benzylium + /Tropylium + Ratios after Charge Transfer to Ethylbenzene

ARTICLE *in* THE JOURNAL OF PHYSICAL CHEMISTRY A · JULY 2004

Impact Factor: 2.69 · DOI: 10.1021/jp031328s

6 AUTHORS, INCLUDING:

Travis D Fridgen
Memorial University of Newfoundland
67 PUBLICATIONS **1,150** CITATIONS
SEE PROFILE

A. A. Viggiano
Air Force Research Laboratory
435 PUBLICATIONS **6,932** CITATIONS
SEE PROFILE

Anthony Midey Jr
Waters Corporation
68 PUBLICATIONS **675** CITATIONS
SEE PROFILE

Terrance Mcmahon
University of Waterloo
206 PUBLICATIONS **5,446** CITATIONS
SEE PROFILE

Experimental and Theoretical Studies of the Benzylium$^+$/Tropylium$^+$ Ratios after Charge Transfer to Ethylbenzene

Travis D. Fridgen*

Department of Chemistry, Wilfrid Laurier University, Waterloo, Ontario, Canada N2L 3C5

Juergen Troe*

Institute for Physical Chemistry, University of Goettingen, Tammannstrasse 6, D-37077 Goettingen, Germany

A. A. Viggiano,* Anthony J. Midey, and Skip Williams

Air Force Research Laboratory, Space Vehicles Directorate, 29 Randolph Road, Hanscom AFB, Massachusetts 017310-3010

Terry B. McMahon

Department of Chemistry, University of Waterloo, Waterloo, Ontario, Canada N2L 3G1

Received: December 17, 2003; In Final Form: February 6, 2004

Benzylium versus tropylium ion yields from the fragmentation of ethylbenzene cations at various excitation energies are studied by forming excited ethylbenzene cations by charge transfer from a series of charge-transfer agents and by identifying the benzylium ion by its secondary reaction with neutral ethylbenzene. At lower excitation energies, the tropylium ion yield decreases with increasing energy from values near 16% (at an energy of 230 kJ mol^{-1}) to 5% (at an energy of 500 kJ mol^{-1}). At higher excitation energies, the tropylium ion yield increases again, which is attributed to secondary isomerization of the vibrationally highly excited benzylium ion arising from the primary fragmentation. It is suggested that this isomerization competes with radiative cooling of the excited benzylium ion. The experimental observations are rationalized in the framework of statistical unimolecular rate theory and electronic structure calculations.

1. Introduction

The production and structures of the prominent mass spectral peak corresponding to $C_7H_7^+$ from various alkylbenzene radical cations and halogen-substituted alkylbenzene radical cations have been the focus of many experimental[1−11] and theoretical[9,10b−d,12−16] studies, and the literature up to 1994 has been comprehensively reviewed.[17] Much of the early work focused on the branching ratios and kinetics of dissociation of the toluene radical cation, or its isomers, into the two main isomers of $C_7H_7^+$—the benzylium and tropylium cations, Bz^+ and Tr^+, respectively.

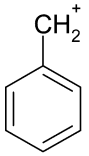

Bz^+

Tr^+

It was possible to determine the composition of the *m*/*z* 91 peak ($C_7H_7^+$) using gas-phase ion chemistry following the discovery that Bz^+ reacts with neutral toluene by exchanging its CH_2^+ with a hydrogen as in Scheme 1.[2]

Following the dissociation of toluene radical cations, forming Bz^+ and Tr^+, the Bz^+ fraction of the *m*/*z* 91 peak would react, leaving only Tr^+. Further investigations showed that Bz^+ also reacts with saturated and unsaturated hydrocarbons as well as with other substituted benzenes such as ethylbenzene.[18]

SCHEME 1

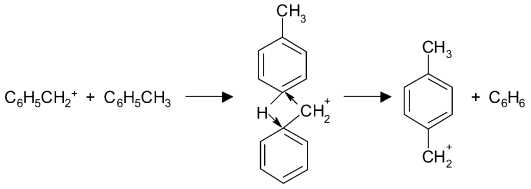

Evolving from this work was the mechanism for the formation of Bz^+ and Tr^+ from ionized and energetic toluene. Bz^+ is formed by simple C−H bond cleavage (eq 1), but Tr^+ is formed by a more tortuous path. The accepted and simplified mechanism for $C_7H_7^+$ production from the toluene radical cation[9] is

$$\text{toluene}^+ \rightarrow Bz^+ + H \quad (1)$$

$$\text{toluene}^+ \rightleftharpoons \text{cycloheptatriene}^+ \quad (2)$$

$$\text{cycloheptatriene}^+ \rightarrow Tr^+ + H \quad (3)$$

Interconversion between the toluene and cycloheptatriene radical cations (eq 2) occurs rapidly at the threshold for hydrogen atom loss.[8,9] Because Tr^+ is thermodynamically preferred over Bz^+, it was puzzling why Bz^+ was formed in fairly high abundance even close to the threshold. According to ab initio calculations,[9]

* To whom all correspondence should be addressed. E-mail: tfridgen@wlu.ca.

10.1021/jp031328s CCC: $27.50
Published on Web 06/02/2004

the answer was that there was a reverse barrier to Tr^+ formation, making the energy requirement for both isomers nearly equal. Statistical modeling[9] of the rate constants for the reactions in eqs 1−3 was found to reproduce experimental Tr^+/Bz^+ ratios following the photodissociation[1] and charge-exchange ionization[3b] of toluene covering a span of about 2−7 eV of internal energy of the toluene radical cation.

Although the understanding of the toluene radical cation system was thought to be complete, some recent mass-analyzed ion kinetic energy spectroscopy (MIKES) experiments[10c] have suggested that the amount of Tr^+ produced from toluene cations dissociating with 3.31 eV of internal is between 75 and 88% of the *m*/*z* 91 intensity, in contrast to the ∼50% established by the earlier photodissociation experiments.[1] The ratios in the MIKES experiments, however, were determined by using statistical phase space theory models to fit kinetic energy release distributions (KERD) that were not clearly bimodal (i.e., consisting of two reaction pathways to the same mass ion). Because of the many assumptions utilized in this determination of Tr^+/Bz^+ ratios, the results should be treated cautiously.

Relatively less investigated is the production of $C_7H_7^+$ from larger alkylbenzenes. $C_8H_{10}^+$ isomers, ethylbenzene ($EtBz^+$), 7-methylcycloheptatriene ($MCHT^+$), and the three xylene (Xl^+) radical cations have been studied. Similar to toluene radical cations isomerizing to cycloheptatriene, it was determined that $EtBz^+$ and $MCHT^+$ isomerize rapidly because the kinetic energy releases were similar for their metastable decompositions producing $C_7H_7^+$.[4] Carbon-13 and deuterium labeling experiments also showed that $EtBz^+$ ions rearrange to yield $MCHT^+$ and some go on further to isomerize to the Xl^+ isomers.[6] Reported in the same work, results of semiempirical calculations showed that Tr^+ was the lowest-energy isomer and was assumed to be the dominant product from the dissociation of the $C_8H_{10}^+$ ions. However, Ausloos found that 80% of the $C_7H_7^+$ dissociation products of energized $EtBz^+$ formed by charge-exchange ionization were due to Bz^+ at energies ∼100 kJ mol^{-1} above the threshold for Tr^+.[3b] Furthermore, he determined that, as with the toluene radical cation, the Tr^+/Bz^+ ratio was dependent on the internal energy of the dissociating $EtBz^+$. In contrast to the toluene radical cation and $EtBz^+$, the metastable *n*-propylbenzene[10b] and *n*-butylbenzene[10a] radical cations were found to produce Bz^+ preferentially. In addition, the rates of fragmentation of excited $EtBz^+$ and Xl^+ at equal internal energies have been found to be quite different.[19]

To investigate further the formation of Bz^+ and Tr^+ from $EtBz^+$ dissociation, $EtBz^+$ was produced with varying amounts of internal energy by charge exchange with different charge-exchange agents. The contributions of Tr^+ and Bz^+ to the *m*/*z* 91 signal was then determined using the method developed by Dunbar[1] and Ausloos.[3b] The brancing ratios were susequently rationalized in terms of statistical unimolecular rate theory.

2. Methods

2.1. ICR Experiments. All ICR experiments were carried out with a Bruker CMS 47 FT-ICR mass spectrometer equipped with a 4.7-T magnet. Vapor from ethylbenzene, EtBz, (99.8%, anhydrous, Aldrich) was degassed using three freeze−pump−thaw cycles and was introduced into the vacuum chamber containing the ion cyclotron resonance (ICR) cell via a precision leak valve. Gaseous Ar, Kr, Xe, N_2, CO, CO_2, O_2, COS, N_2O, and vapor from CS_2 (also degassed) were introduced into the vacuum chamber containing the ICR cell through a separate precision leak valve. The pressure inside the ICR vacuum chamber was measured with an ionization gauge. The ionization

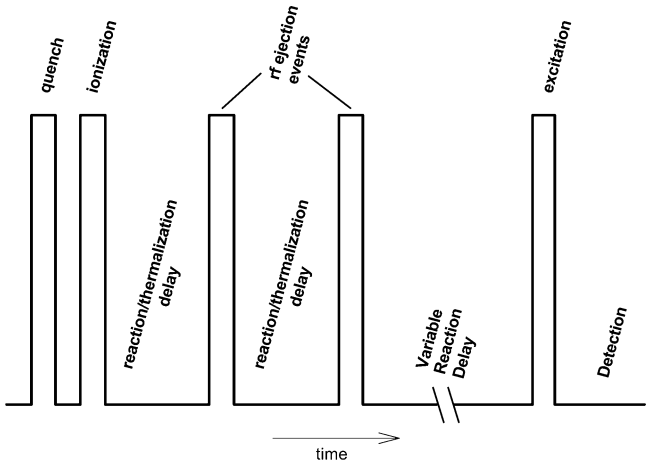

Figure 1. Scan function for the FT-ICR experiments conducted in this work.

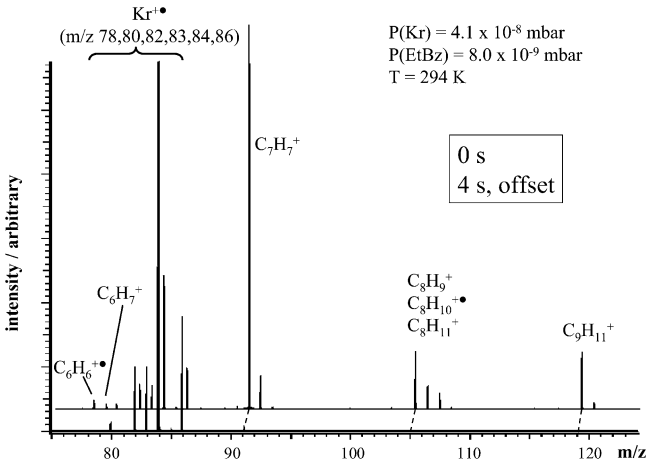

Figure 2. Mass spectra recorded after no delay and a 4-s delay showing the reaction of Kr^+ with neutral EtBz.

gauge was calibrated for EtBz by using the reaction of EtBz with O_2^+, which is known to occur at the capture rate[11d,e] given by the Su and Chesnavich[20] capture rate constant. The pressure of EtBz was on the order of 10^{-8} mbar for all experiments, and the pressure of the charge-exchange (CE) agent in the ICR cell was between 2 and 10 times this amount ($>10^{-7}$ mbar)

Ionization was done directly inside the ICR cell using 50−100-ms pulses of 70-eV electrons. Delays prior to the variable delay (see scan function, Figure 1) were incorporated to ensure thermalized reactant ions and, when determining the composition of the $C_7H_7^+$ (*m*/*z* 91) ions, to allow enough time to form $C_7H_7^+$ by the reaction of EtBz with the CE agent by the general reaction shown in eq 4.

$$M^+ + EtBz \rightarrow M + EtBz^{+}* \rightarrow M + C_7H_7^+ + CH_3 \quad (4)$$

Following each delay, desired ions could be isolated by ejecting undesired ions by standard rf ejection techniques. The relative ion intensities were determined after variable reaction delays during which the isolated ions were allowed to react with the neutral background gas. Examples of mass spectra obtained for the reaction of Kr^+ with EtBz are shown in Figure 2. The corresponding semilogarithmic plot of normalized ion intensity versus time is shown in Figure 3. All experiments were done at room temperature, which was 294 K.

The details of the kinetics analyses and the determination of Bz^+ and Tr^+ contributions to the *m*/*z* 91 peak in the ICR experiments are given below in section 3.2.

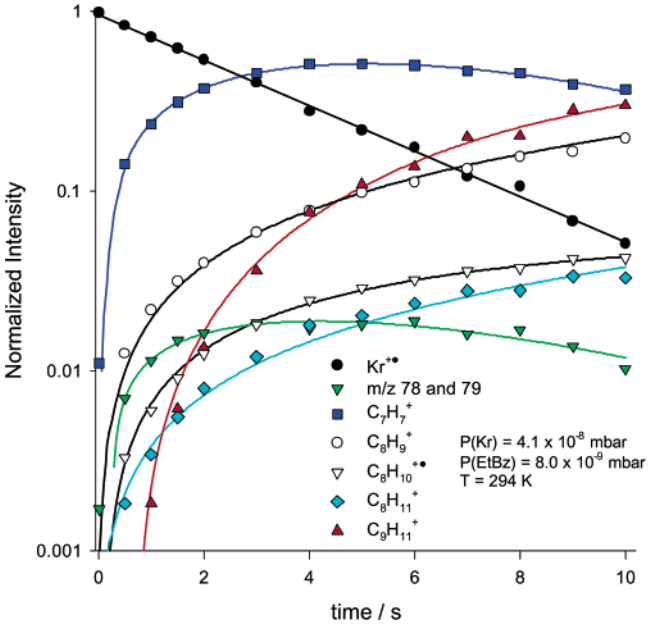

Figure 3. Semilogarithmic plot of normalized ion intensity vs time for the reaction of Kr^+ with neutral EtBz.

2.2. SIFT Experiments. The selected ion flow tube (SIFT) is described in detail elsewhere,[21] and only pertinent information is summarized here. O_2^+ is generated by electron impact on O_2 in an effusive ion source in a high-pressure source region. A flow of O_2 (2 cm^3 s^{-1}) is added 30 cm upstream of the reaction region to quench O_2^+ electronic[22] and vibrational[23] excited species. For the SIFT experiments, the product distributions were determined as follows. The overall branching ratios are measured by extrapolating the normalized product branching ratios from a kinetics run to zero ethylbenzene flow to get the total fraction of *m*/*z* 91, $f_{91\ tot}$. The maximum concentration of C_8H_{10} has been restricted to minimize the secondary reaction of $C_7H_7^+$, thus minimizing the slope of the extrapolation and ensuring the most accurate value for $f_{91\ tot}$. Next, the branching ratios are recorded at the maximum possible C_8H_{10} concentrations. Keeping the flow-tube pressure at 1 Torr allows the highest reaction time and allows Bz^+ to be fully depleted at the highest reactant flows. This condition is indicated by a plateau in the *m*/*z* 91 product signal as a function of ethylbenzene flow at high C_8H_{10} flow. At this point, the fraction of the *m*/*z* 91 products remaining, $f_{91\ max\ EtBz}$, reflects only the Tr^+ isomer. Consequently, the percent of *m*/*z* 91 having the Tr^+ structure can be given by eq 5.

$$\%\ Tr^+ = \frac{f_{91\ max\ EtBz}}{f_{91\ tot}} \times 100\% \qquad (5)$$

It should be noted that the branching ratios have been corrected for an ~5% H_3O^+ impurity in the flow tube, which produces only $C_8H_{11}^+$ at 298 K.[11c] This impurity persisted despite trapping the He buffer with a sieve trap to remove water vapor. This correction was necessary because of the low resolution settings used to minimize mass discrimination.

2.3. Electronic Structure Calculations. To characterize the reaction paths relevant to the present study at least semiquantitatively, a series of electronic structure calculations were made. Structures were optimized and vibrational frequencies were calculated at the B3LYP level of theory employing the 6-31+G** basis set. Single-point calculations were made at the MP2 level of theory employing the same basis set and at the B3LYP level using the larger 6-311+G(2df,p) basis set on the B3LYP/6-31+G** optimized structures. The relative enthalpies reported as MP2/6-31+G**//B3LYP/6-31+G** or B3LYP/6-311+G(2df,p)//B3LYP/6-31+G** are composed of these MP2/6-31+G** or B3LYP/6-311+G(2df,p) electronic energies, respectively, and are corrected for zero-point and thermal contributions to the enthalpy using the B3LYP/6-31+G* vibrational frequencies.

Optimizing some transition-state geometries at the MP2 level of theory proved to be virtually impossible so that G3-type calculations were not possible. Therefore, a variation of G3MP2[24] calculations was made. The modification was that instead of using HF frequencies for the zero-point and thermal-energy contributions the B3LYP/6-31+G** vibrational frequencies were used. Also, instead of optimizing the structures at the MP2 level of theory as is done for G3MP2 calculations, the B3LYP/6-31+G** optimized geometries were used for the high-level single-point calculations. Therefore, the MP2(FC)/G3MP2large, MP2(FC)/6-31G* and QCISD(T,FC)/6-31G* single-point energies were calculated for the B3LYP/6-31+G** optimized geometries. These substituted energies, then, were used exactly as prescribed by the G3MP2 formalism. This modified version of G3MP2 will be termed spG3MP2 in the rest of this paper.

Transition states were characterized by the presence of an imaginary vibrational frequency with the correct nuclear motion corresponding to the reaction coordinate. No effort was made to include the basis set superposition error (BSSE), but on the basis of the modest size of the basis set used, BSSE is expected to be minimal. All calculations were made using the Gaussian 98 suite of programs.[25]

2.4. Statistical Rate Calculations. Benzylium ions are formed by simple bond fission of vibrationally highly excited $EtBz^+$. The specific rate constants $k(E)$ for this process have been measured.[10d,19] They have also successfully been modeled by statistical rate calculations[26] using SACM/CT (statistical adiabatic channel model/classical trajectory) calculations applied to a short-range valence/long-range electrostatic potential suitable for simple molecular ion fragmentation. Tr^+ ions under the present low-pressure conditions can be formed in two ways, either directly by the fragmentation of $EtBz^+$ on a pathway involving a reverse barrier or by the secondary isomerization of highly vibrationally excited Bz^+ ions originating from the primary fragmentation of $EtBz^+$ giving $Bz^+ + CH_3$. As a start, we have modeled $k(E)$ for the primary formation of Tr^+ from $EtBz^+$ by standard rigid activated complex RRKM theory using transition-state parameters from the calculations of section 2.3. Because this approach did not succeed in reproducing the measured Tr^+/Bz^+ yields, the treatment had to be modified as described below.

To calculate the secondary isomerization of Bz^+ to Tr^+, the energy partitioning between the fragments of the primary dissociation of $EtBz^+$ to Bz^+ and CH_3 was calculated by statistical methods. For each slice of the energy distribution of excited Bz^+, the rate of the isomerization of Bz^+ to Tr^+ was estimated by standard rigid activated complex RRKM theory using transition-state parameters from the calculations described in section 2.3. This calculation again was found not to be consistent with the experimental results; see section 4. Because only a small fraction of excited Bz^+ ended up as Tr^+ in our experiments, there had to be a process competing with Bz^+ isomerization, thereby preventing the transformation of Bz^+ to Tr^+. At low pressures (10^{-8}−10^{-7} mbar) and during the long reaction times (between 50 and 100 s) of our experiments, this

TABLE 1: Calculated Collision Rate Constants and Experimental Rate Constants for Charge-Exchange Reactions[a] between Ethylbenzene and the Indicated Radical Cations

CE agent	$k_{c,calcd}$[b]/ 10^{-9} cm^3 s^{-1}	$k_{c,exptl}$/ 10^{-9} cm^3 s^{-1}	difference/%
CS_2^+	1.43	1.24	−15.3
COS^+	1.54	1.42	−8.5
O_2^+	1.92	2.0[c]	4.0
Xe^+	1.25	1.13	−10.6
N_2O^+	1.71	1.66	3.0
CO_2^+	1.71	1.79	4.5
Kr^+	1.39	1.47	5.4
CO^+	2.03	[d]	
N_2^+	2.00	1.92	−4.2
Ar^+	1.77	1.87	5.3

[a] The charge-exchange reaction leading to $EtBz^+$ and its dissociation products. [b] Ion−dipole collision rate from ref 20. [c] Experimental value taken from ref 11e. [d] No data.

process was postulated to be radiational cooling of Bz^+ by IR emission. The amount of $Bz^+ \rightarrow Tr^+$ conversion observed at the highest studied excitation energies could be rationalized at least semiquantitatively as discussed below.

3. Results and Discussion

3.1. Charge-Exchange Reactions. Because of the inability to measure absolute pressures using the ionization gauge, it is necessary to calibrate. The rate constant for the charge-exchange reaction of O_2^+ with EtBz has been found[11] to be 2.0×10^{-9} cm^3 s^{-1}, which is very close to the Su and Chesnavich[20] capture rate constant of 1.92×10^{-9} calculated at 294 K using 0.59 D and 14.2×10^{-24} cm^3 as the dipole moment and polarizability, respectively, of neutral EtBz. This reaction rate constant was used to generate the ionization gauge calibration factor of 0.80 ± 0.07 for determining the pressure of EtBz in the ICR cell. The pressure read from the ion gauge is multiplied by this factor to yield the true pressure of EtBz.

In Table 1 are listed the capture rate constants as well as the rate constants determined experimentally (calibrated by O_2^+ + EtBz) and the percent deviation of the two values. It is clearly evident that the charge-exchange reaction occurs essentially on every collision between EtBz and the charge-exchange agent because most of the measured rate constants deviate from the collision rate by less than 10% and many by less than 5%. The most significant difference between the calculated collision rate constant and the measured charge-exchange rate constant is for the reaction of CS_2^+ with EtBz, which is 15% lower than the calculated collision rate. It is interesting that the only product of this reaction is $EtBz^+$. No dissociation occurs because the maximum internal energy that can be imparted to $EtBz^+$ is 125 kJ mol^{-1}, which is less than the expected dissociation energy based on previous ab initio calculations.[10d] However, the charge-exchange reaction is 125 kJ mol^{-1} exothermic, and there is no reason to expect it to occur at other than the capture rate.

3.2. Reaction of *m/z* 91 and Fractions of Tropylium and Benzylium Cations. Dunbar[1] showed that the amount of Tr^+ comprising *m/z* 91 formed following the ionization of toluene could be quantified because the Bz^+ component of *m/z* 91 reacted with neutral toluene, yielding an ion at *m/z* 105 and, presumably, benzene as in Scheme 1. Later, Ausloos[3b] showed that a similar reaction between Bz^+ and EtBz (eq 6) could be utilized to quantify the amounts of the two isomers following the ionization of EtBz.

$$\underset{m/z\ 91}{C_8H_5CH_2^+} + C_6H_5CH_2CH_3 \rightarrow \underset{m/z\ 119}{CH_3CH_2C_6H_4CH_2^+} + C_6H_6 \quad (6)$$

This approach to quantifying Bz^+ and Tr^+ from $EtBz^+$ dissociation was taken in the present study.

In Figure 4 are shown mass spectra after 0, 20, and 55 s of reaction time, and in Figure 5 is the normalized ion intensity versus time profile. The pulse sequence used to generate these mass spectra included an initial delay of ∼2 s, after which all ions except those corresponding to Kr^+ were ejected. Then, a second delay of ∼3 s was incorporated to allow the charge-exchange reaction to occur, during which large amounts of *m/z* 91 as well as some other products, as seen in Figures 2 and 3, were produced. It can be seen from Figure 4 that the spectrum recorded after 0 s delay (i.e., generated immediately following the second ejection event) contains signals due to ions of *m/z* 105, 106, 107, 119, and 120 as well as the $C_7H_7^+$ ions at *m/z* 91 and 92. The ion at *m/z* 119 is the product of the reaction shown in E. 6, and the ion at *m/z* 120 is the ^{13}C contribution. The ion at *m/z* 106 is the molecular ion formed upon CE, and *m/z* 107 is likely a product of the proton-exchange reaction from $C_6H_7^+$ (*m/z* 79) to EtBz (eq 7).

$$\underset{m/z\ 79}{C_6H_7^+} + C_6H_5CH_2CH_3 \rightarrow C_6H_6 + \underset{m/z\ 107}{C_8H_{11}^+} \quad (7)$$

The ions at *m/z* 106 and 107 are neither produced nor react, as is evidenced by the fact that their relative intensities remain constant during the course of the experiment following the second ejection event. That these ions are not simply isotopomers comes from their relative intensities. As is easily seen from Figure 4, the *m/z* 107 peak is about 25% of the *m/z* 106 peak. If the ^{13}C contribution from $C_8H_9^+$ (*m/z* 105) to *m/z* 106 is subtracted, then the peak at *m/z* 107 is about 70−80% of the $C_8H_{10}^+$ signal. If the peak at *m/z* 107 were the ^{13}C contribution from $C_8H_{10}^+$, it would be only 8.9% of the intensity due to $C_8H_{10}^+$. These ions were not ejected because of their close proximity to the *m/z* 105 ion, which we did not want to disturb. (See below.)

Ausloos attributed the ion at *m/z* 105 to a product of the minor hydride exchange reaction of Bz^+ with neutral EtBz, where the transferred hydride ion was shown from labeling experiments to originate from the α position of EtBz.[3b]

$$\underset{m/z\ 91}{C_7H_7^+} + C_6H_5CH_2CH_3 \rightarrow C_7H_8 + \underset{m/z\ 105}{C_6H_5CHCH_3^+} \quad (8)$$

Although we cannot rule out the occurrence of the reaction in eq 8, it is clear from Figure 5 that the ion produced from the reaction of Bz^+ and EtBz in eq 6, *m/z* 119, is depleted at long times and reacts, most likely with neutral EtBz, according to the hydride-exchange reaction given in eq 9, to form the ion at *m/z* 105:

$$\underset{m/z\ 119}{CH_3CH_2C_6H_4CH_2^+} + C_6H_5CH_2CH_3 \rightarrow CH_3CH_2C_6H_4CH_3 + \underset{m/z\ 105}{C_6H_5CHCH_3^+} \quad (9)$$

This conclusion is still consistent with Ausloos' labeling studies and is our preferred explanation for the presence of *m/z* 105. It was possible to obtain good fits for the $C_9H_{11}^+$ (*m/z* 119, red curve in Figure 5) intensity versus time data and obtain a rate constant for the hydride-transfer reaction given in eq 9. Our

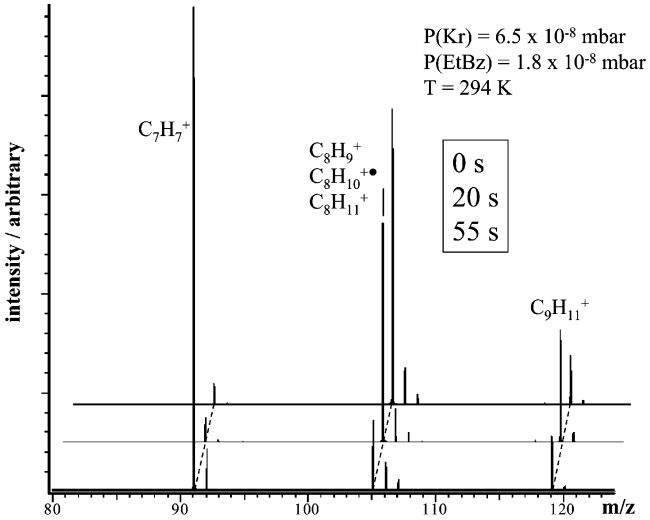

Figure 4. Mass spectra recorded after no delay as well as after 20- and 55-s delays following the isolation of ions at *m/z* 91, 91, 105, 106, 107, 119, and 120. These delays followed the 4-s reaction of Kr^+ with neutral EtBz.

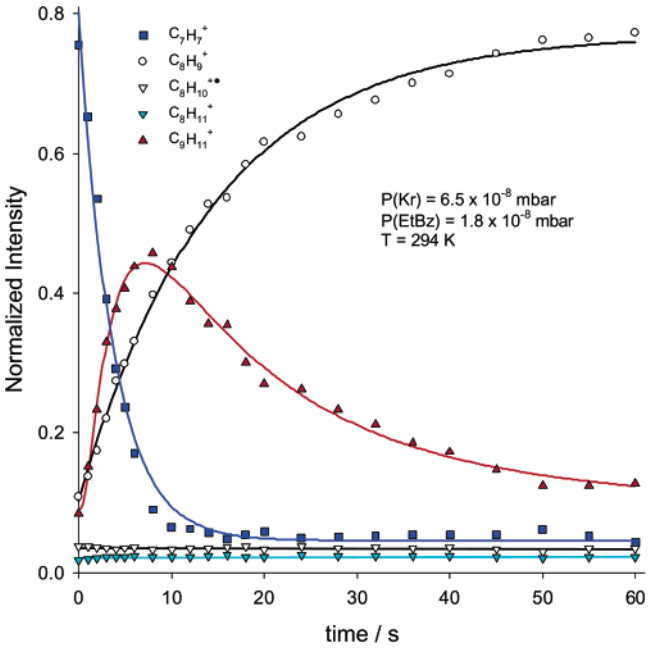

Figure 5. Plot of normalized intensity vs time for the reaction of the Bz^+ fraction of the *m/z* 91 signal with neutral EtBz. This kinetics plot corresponds to the mass spectra in Figure 4.

experimental value for this rate constant is $8.1(\pm1.4) \times 10^{-11}$ cm^3 s^{-1}. The B3LYP/6-31+G** calculations predict this reaction to be exothermic by 21 kJ mol^{-1}. The fact that this hydride-exchange reaction occurs only at about 5% of the collision rate (1.3×10^{-9} cm^3 s^{-1}) is most likely due to the presence of a central barrier that occurs because of the rehybridization of the hydride donating and receiving carbon atoms.

Now, by allowing the ions at *m/z* 105, 106, 107, 119, and 120 to remain along with the $C_7H_7^+$ ions allows us to quantify the reactive and nonreactive contributions to the $C_7H_7^+$ signal (i.e., to Bz^+ and Tr^+, respectively). This includes the Bz^+ that reacts at very short times. The $\%Tr^+$ is then given by

$$\% \mathrm{Tr}^+ = \frac{[\mathrm{Tr}^+]}{[\mathrm{Tr}^+] + [\mathrm{Bz}^+]} \times 100\% = \frac{f_{91,\infty}}{1 - f_{106+107}} \times 100\% \quad (10)$$

TABLE 2: Rate Constants for the Reaction of the Benzylium Cation with Ethylbenzene[a] for the Different CE Agents Used

CE agent	rate constant/ 10^{-10} cm^3 s^{-1}
COS^+	6.1 (±0.8)
O_2^+	5.0 (±0.6)
Xe^+	5.6 (±0.6)
N_2O^+	6.1 (±1.3)
CO_2^+	6.3 (±0.7)
Kr^+	6.1 (±0.5)
CO^+	5.4 (±0.6)
N_2^+	6.1 (±0.6)
Ar^+	5.9 (±1.3)

[a] Equation 6.

TABLE 3: Tropylium$^+$ Component of the *m/z* 91 Peak Formed Following the Charge-Exchange Reaction with Ethylbenzene

CE agent	EA of CE agent[a]/eV	E_{int}/eV (kJ mol^{-1})	Tr^+ yield (Y)/% this work	Tr^+ yield (Y)/% Ausloos[b]
CS_2^+	10.073	1.30 (125)	0	
COS^+	11.18	2.41 (233)	15.8 (±0.4)	15
O_2^+	12.071	3.30 (318)	10.2 (±0.3)	
Xe^+	12.13	3.36 (324)	7.5 (±0.2)	12
N_2O^+	12.889	4.12 (397)	5.2 (±0.3)	
CO_2^+	13.77	5.00 (482)	4.7 (±0.4)	
Kr^+	14.000	5.23 (505)	5.1 (±0.5)	11
CO^+	14.000	5.23 (505)	5.5 (±0.2)	
N_2^+	15.576	6.81 (657)	14.9 (±0.2)	
Ar^+	15.760	6.99 (674)	16.4 (±0.2)	20

[a] Electron affinity based on the ionization potential of the neutral. [b] Estimated from Figure 2 of ref 3b.

where $f_{91,\infty}$ is the fraction of *m/z* 91 remaining at infinite time (i.e. after Bz^+ reacts away), and $f_{106+107}$ is the fraction of *m/z* 106 and 107 that remains constant. For the particular experiment represented in Figure 5, $f_{91,4} = 0.046$ and $f_{106+107} = 0.056$, yielding a Tr^+ contribution to *m/z* 91 of 4.9%.

The decay of the $C_7H_7^+$ signals was well represented by a double exponential

$$I_{C_7H_7^+} = ae^{-k_1't} + be^{-k_2't} \quad (11)$$

where *a* and *b* are the intensities of the Bz^+ and Tr^+, respectively, at zero time. The value of *b* is equivalent to $f_{91,\infty}$ above. The pseudo-first-order rate constants, k_1' and k_2', are the rates of decay of Bz^+ and Tr^+ signals, respectively. Assuming that the only way these signals decay is by the reaction with neutral EtBz (i.e., eq 5), dividing k_1' and k_2' by the corrected EtBz pressure yields the rate constants for the reaction of these ions with EtBz. All second-order rate constants determined in this way for Tr^+ decomposition (k_2) were less than 10^{-18} cm^3 s^{-1}, showing that Tr^+ is virtually unreactive. The rate constants determined for the Bz^+ ion fraction are listed in Table 2 and are fairly constant, with an average value of about 5.8×10^{-10} cm^3 s^{-1}, which is 1 of about every 2.4 collisions because the capture rate constant is 1.36×10^{-9} cm^3 s^{-1}. The rate constants listed in Table 2 are in very good agreement with $6.5(\pm0.1) \times 10^{-10}$ cm^3 s^{-1} measured by Ausloos.[3b]

In Table 3 are listed the Tr^+ contributions to *m/z* 91 formed according to eq 4 for the various charge-exchange agents used. Also shown are the values obtained by Ausloos,[3b] and it is apparent that these values are higher than those determined in the present study. Ausloos states that these values are an upper estimate of the Tr^+ contribution.[28] The likely source of the difference is the neglect of Bz^+, which reacts at short times so

that the $C_7H_7^+$ ions sampled in Ausloos' study are already slightly depleted of Bz^+. In the present study, as described above, care was taken not to eject any of the Bz^+ reaction products, *m*/*z* 119 and 105, and care was taken to include them to get an accurate determination of the $\%Bz^+$ and $\%Tr^+$.

The 10.2% Tr^+ observed in the current ICR experiments for the reaction with O_2^+ disagrees with the previous measurement of 33% Tr^+ found in a selected ion flow tube (SIFT) for this reaction at 298 K.[11a] In light of this disagreement, we have made new SIFT measurements. The branching fractions for the current O_2^+ SIFT measurements are 0.36 $C_8H_{10}^+$, 0.61 $C_7H_7^+$ (total), and 0.03 $C_6H_6^+$, in agreement with the previous SIFT results within the 10% relative error of the product determinations in that study.[11a] The current measurements have been made with a flow tube pressure of 1 Torr, which is twice the pressure used previously. The amount of Tr^+ from the current SIFT measurements is 18%, much less than the 33% previous SIFT measurement[11a] and in much better agreement with the current ICR value of 10% as well as the Ausloos value of 15%.[2] A key difference is that the current SIFT determination was made using the difference in the *m*/*z* 91 peak for differing amounts of C_8H_{10}. Previously, the amount of Tr^+ was determined by the increase in the products from the secondary chemistry observed in the plateau region; therefore, mass discrimination may have played a role in the earlier experiments, despite attempts to operate the mass spectrometer under favorable conditions. In the current SIFT measurements, relative values of the same mass peak under a fixed set of resolution settings gives the $\%Tr^+$, so there is less of a problem with mass discrimination in the present experiment. However, there is still a small but significant difference between the ICR and SIFT values, but the currently better agreement gives us confidence that we are measuring the same quantity. The remaining discrepancy may stem from the fact that the Bz^+ fraction of the *m*/*z* 91 signal clusters with EtBz in the high-pressure SIFT experiments to form an ion at *m*/*z* 197 rather than by the reaction in eq 6 as in the very low pressure ICR experiments. Therefore, it is conceivable that a certain fraction of the *m*/*z* 197 ions fragment back to *m*/*z* 91 prior to being detected and are therefore recorded, mistakenly, as Tr^+.

In Figure 6, the $\%Tr^+$ is plotted against the internal energy of the $EtBz^+$ generated by charge exchange. It is apparent that the amount of Tr^+ at low energies decreases with increasing internal energy but that increasing the internal energy of $EtBz^+$ above 5−6 eV results in a leveling off and a marked increase in the Tr^+ signal. This has been attributed[3b] to reaching a point where Bz^+, formed by the loss of CH_3 from $EtBz^+$ (or the loss of H from the toluene radical cation), has enough energy to isomerize to Tr^+. By an extrapolation of these two seemingly linear relations (low energy and high energy), it is found that they cross at 4.57 eV. This value could be taken as the threshold for Bz^+/Tr^+ isomerization from $EtBz^+$. In fact, this threshold was calculated to be 4.59 eV at both the B3LYP/6-311+G(2df,p)//B3LYP/6-31+G** and spG3MP2 levels of theory (see below).

3.3. Analysis of Primary Tr^+ Yields. The fragmentation of vibrationally highly excited $EtBz^+$ can lead either to Tr^+ or to Bz^+ via two competing unimolecular dissociation reactions:

$$EtBz^+ \rightarrow Bz^+ + CH_3 \qquad (12)$$

$$EtBz^+ \rightarrow Tr^+ + CH_3 \qquad (13)$$

The energy dependence of the sum of the two specific rate constants, where the subscripts in eq 14 refer to the reactions in eqs 12 and 13,

$$k(E) = k_{12}(E) + k_{13}(E) \qquad (14)$$

has been investigated in detail before, both experimentally[10d,19] and theoretically,[11e,26] at least for the dominant part, $k_{12}(E)$. It was shown in ref 11e that a knowledge of $k(E)$ allows the quenching of dissociation by large bath-gas pressures to be analyzed quantitatively with respect to the collisional quenching rate. In the present case, the knowledge of $k(E)$ allows the derivation of $k_{13}(E)$ from the measured $[Tr^+]/([Tr^+]+[Bz^+])$ yields through

$$k_{13}(E) = \left(\frac{[Tr^+]}{[Tr^+]+[Bz^+]}\right)k(E) \qquad (15)$$

Equation 15 holds for experiments with charge-exchange agents having ionization potentials less than about 13 eV. With the other agents, the secondary formation of Tr^+ from Bz^+ also has to be taken into account. It was shown in ref 11e that $k(E)$, for $k(E) \geq 10^3\ s^{-1}$, can be expressed in analytical form by

$$k(E) = 1.6 \times 10^8\ s^{-1}\left[\frac{E - E_o}{219.5\ kJ\ mol^{-1}}\right]^{4.824} \qquad (16)$$

where $E_o = 168.3\ kJ\ mol^{-1}$ denotes the $EtBz^+$ dissociation energy for reaction 12. Using the present results for the Tr^+ yield from Table 3 leads to experimental values of $k_{13}(E)$, which are given in Table 4.

Obviously, the derived values for $k_{13}(E)$ can only be as accurate as the values of $k(E)$ from eq 16. In addition, we also assume that the energy E is sufficiently close to the 0 K reaction enthalpy for charge exchange. A complete discussion of charge-transfer mechanisms and of energy partitioning is given in ref 11e. The small values of the Tr^+ yields indicate that, despite

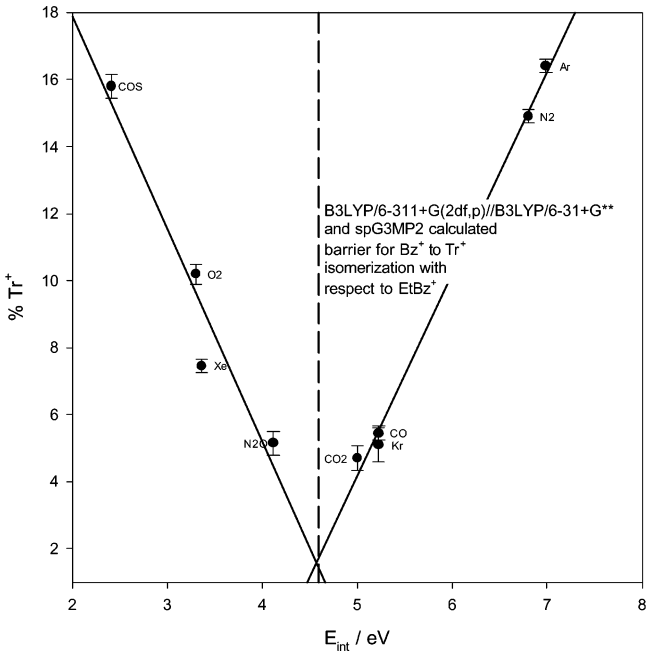

Figure 6. Plot of the experimentally derived %Tr making up the *m*/*z* 91 signal vs internal energy. On the plot are the neutral charge-exchange agents used to ionize the neutral precursor, EtBz. Also shown are lines drawn through the two linear parts of the data at high and low energy. The dashed line is the energy threshold for the isomerization of Bz^+ to Tr^+ with respect to $EtBz^+$.

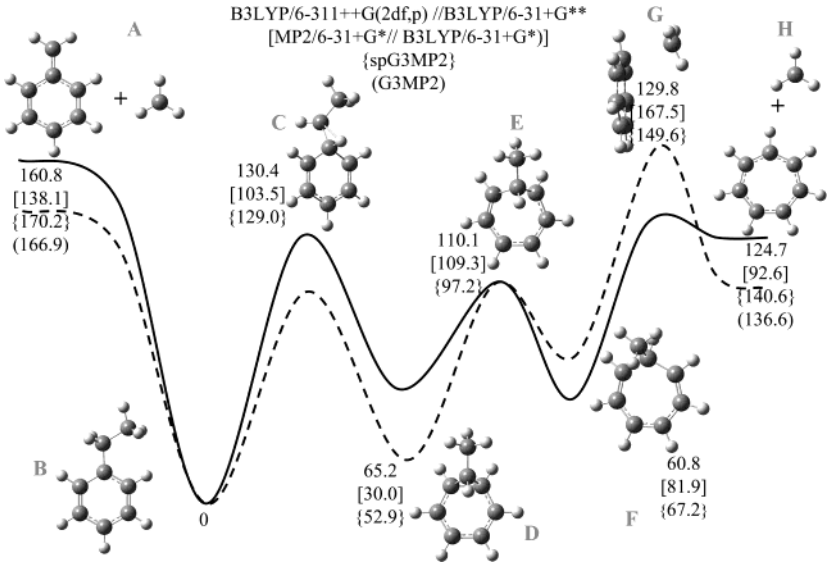

Figure 7. Calculated potential energy profiles for the lowest-energy route to the two $C_7H_7^+$ isomers, Bz^+ and Tr^+, from $EtBz^+$; see the text for details. The dashed line corresponds to the MP2-calculated energies, which differ significantly from the others to warrant their inclusion.

TABLE 4: Dissociation Rate Constants for Excited Ethylbenzene Radical Cations

CE agent	E_{int}/eV (kJ mol^{-1})	$k(E)^a$/s^{-1}	$k_{13}(E)_{exp}{}^b$/s^{-1}	$k_{13}(E)_{mod}{}^c$/s^{-1}
COS^+	2.41 (233)	5.6×10^5	8.8×10^4	9.3×10^4
O_2^+	3.30 (318)	2.6×10^7	2.7×10^6	2.3×10^6
Xe^+	3.36 (324)	3.1×10^7	2.3×10^6	2.6×10^6
N_2O^+	4.12 (397)	2.2×10^8	1.1×10^7	1.2×10^7
CO_2^+	5.00 (482)	1.2×10^9	5.3×10^7	3.7×10^7
Kr^+	5.23 (505)	1.3×10^9	6.4×10^7	4.6×10^7
CO^+	5.23 (505)	1.3×10^9	6.9×10^7	4.6×10^7
N_2^+	6.81 (657)	7.6×10^9	1.1×10^9	1.6×10^8
Ar^+	6.99 (674)	9.0×10^9	1.5×10^9	1.8×10^8

[a] Total rate constants from eq 16. [b] Apparent rate constant for Tr^+ formation from eq 15. [c] Modeled rate constant for Tr^+ formation from scaled B3LYP/RRKM calculations; see the text for details.

the smaller dissociation energy for $EtBz^+$ in reaction 13 in comparison to that in reaction 12, $k_{12}(E)$ is more than a factor of 5 larger than $k_{13}(E)$ over the energy range studied. This can be explained only by the existence of a reverse barrier for reaction 13, which is accompanied by a rigid activated complex in contrast to the relatively loose activated complex in reaction 12. In the following discussion, we will try to provide a more quantitative analysis of this situation. We do this on two levels: by RRKM modeling starting with parameters from B3LYP/6-31+G** calculations and then fitting the threshold energy E_o and frequency parameters for reaction 13 to reproduce the experiments and by totally empirical fitting.

We illustrate the calculated minimum-energy path of competing reactions 12 and 13 in Figure 7. Three types of calculations are shown: MP2/6-31+G**//B3LYP/6-31+G** (dashed line), B3LYP/6-311+G(2df,p)//B3LYP/6-31+G** results (solid line), and spG3MP2. The thermodynamic dissociation energies for the two channels at 0 K are about 127 kJ mol^{-1} for reaction 13 and 168 kJ mol^{-1} for reaction 12. (See Figure 7 and refs 10d and 28[29] for the conversion from 298 to 0 K.) The value for reaction 13 from ref 24 is not very different from the DFT or the spG3MP2 results of Figure 7 supporting the energetics calculated by this approach. (The MP2 results appear to be much less satisfactory.) Nevertheless, the energetic parameters are not sufficiently precise for quantitative rate calculations. The same applies to the frequency parameters. Although the results from the B3LYP calculations for stable structures often proved realistic after suitable scaling,[30] less is known about the

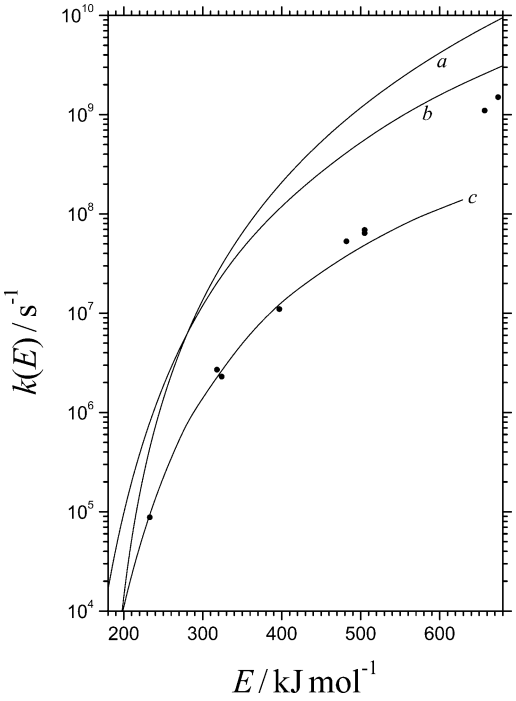

Figure 8. Specific rate constants for the dissociation of $EtBz^+$ to Bz^+ and Tr^+. (a) Dissociation to $Bz^+ + Tr^+$ from eq 16; (b) dissociation to Tr^+, modeling with unscaled transition-state frequencies from B3LYP calculations; (c) dissociation to Tr^+, modeling with scaled transition state frequencies; see the text and eq 18; (●) apparent experimental rate constants $k_{13}(E)$ from eq 15.

frequencies calculated for the transition-state structures, especially the low-frequency modes. Appendix A gives our B3LYP frequency sets for various structures included in Figure 7.

In Figure 8, $k(E)$ from eq 16 (curve a) and the apparent values for $k_{13}(E)$ from eq 15 (points) are shown. At first we compared the derived $k_{13}(E)$ with values modeled by rigid activated complex RRKM theory, using $E_0 = 129.8$ kJ mol^{-1} and $EtBz^+$ and transition-state (structure G) frequencies unscaled from B3LYP calculations. The derived $k_{13}(E)$ at $E = 310$ kJ mol^{-1} exceeds the measurements by about a factor of 70. Repeating this modeling for structure C does not change this picture. For this reason, we have to employ parameter fitting. Unfortunately, the modeled $k(E)$ is very sensitive to the global scaling factors

for the B3LYP frequencies. Expressing $k(E)$ in the form $k(E) = W(E)/h\rho(E)$, the density of states, $\rho(E)$, at $E = 310$ kJ mol^{-1} scales with a global scaling factor F for the B3LYP frequencies of $EtBz^+$ according to $\rho(E) \propto F^{-26}$. The number of states, $W(E)$, also scales according to $W(E) \propto F^{\ddagger \text{ThinSpace}-19}$, where $F^{\ddagger}$ denotes a global factor for the B3LYP frequencies of the transition state. Unfortunately, the very sensitive dependencies of $\rho(E)$ and $W(E)$ on F and on $F^{\ddagger}$ and the failure of $k(E)$ modeling with unscaled B3LYP frequencies mean that the modeling becomes a mere parameter fitting. The dependencies indicated that $F^{\ddagger}$ should be greater than 1, F should be less than 1, and $\rho(E)$ should increase. This results in a decrease of $k(E)$. We arbitrarily chose $F = 0.9$ for the $EtBz^+$ frequencies, such as those observed by a comparison of B3LYP and experimental frequencies for *trans*-stilbene[30−32] in the low- to medium-frequency range. To fit to the experimental values, we then had to tighten up the B3LYP transition-state frequencies by a global scaling factor $F^{\ddagger} = 1.09$ and increase E_0 by a factor of 1.05 to $E_0 = 136.7$ kJ mol^{-1}. In Figure 8, it is demonstrated that the apparent experimental $k_{13}(E)$ values for the lower-energy CE agents COS^+, O_2^+, Xe^+, and N_2O^+ now are well reproduced. The apparent experimental $k_{13}(E)$ for the higher-energy CE agents CO_2^+, Kr^+, CO^+, N_2^+, and Ar^+ are increasingly underestimated, which is attributed to the secondary isomerization of Bz^+. Instead of using a global scaling factor, one could also have scaled a group of frequencies or a single frequency, or one could have changed the reaction coordinate. However, this would not appreciably change the modeled $k_{13}(E)$. The results of our modeling are included in Table 4.

It has been shown that, for systems of comparable molecular size to those considered here, $k(E)$ can be very well represented empirically by the form

$$k(E) \propto (E - E_0)^{s-1} \tag{17}$$

with an empirical value for the exponent s.[33] Equation 16 is an example of this form with $s = 5.824$. The unscaled DFT modeling of $k_{13}(E)$ can also be represented by eq 17 with $s = 6.825$. Fitting the experimental $k_{13}(E)$ in Figure 8 to the form of eq 17 for $s = 5.824$ yields $E_0 = 136.7$ kJ mol^{-1}, and for $s = 6.825$, $E_0 = 104.8$ kJ mol^{-1} is obtained. The empirical fitting, therefore, yields E_0 values that are close to the DFT results and the RRKM fitting, provided that s is limited by the range of values given above. $k_{13}(E)$ in this way can be approximated by

$$k_{13}(E) = 1.26 \times 10^7 \text{ s}^{-1}\left[\frac{E - E_0}{260.8 \text{ kJ mol}^{-1}}\right]^{4.824} \tag{18}$$

with $E_0 = 136.7$ kJ mol^{-1}. On the basis of our two methods of fitting, in the worst case, this value is estimated to be uncertain by ±30 kJ mol^{-1}. This expression is used in the next section to separate the primary and secondary formation of Tr^+ at higher excitation energies.

3.4. Analysis of Secondary Tr^+ Yields. Independent of the question of which modeling of $k_{13}(E)$ appears most appropriate, one estimates a primary Tr^+ yield for the energies of the CO_2^+, Kr^+, and CO^+ experiments of about 4% and for the energies of the N_2^+ and Ar^+ experiments of only 3%. For the N_2^+ and Ar^+ experiments, this implies that more than 80% of the Tr^+ must come from a secondary isomerization:

$$Bz^+ \rightarrow Tr^+ \tag{19}$$

The question arises as to why the remaining Bz^+ has also not isomerized. To answer this question, the energy content of the Bz^+ formed by reaction 12 has to be specified, the specific rate constant $k_{19}(E)$ has to be estimated, and a quenching process, which could suppress reaction 19, needs to be identified.

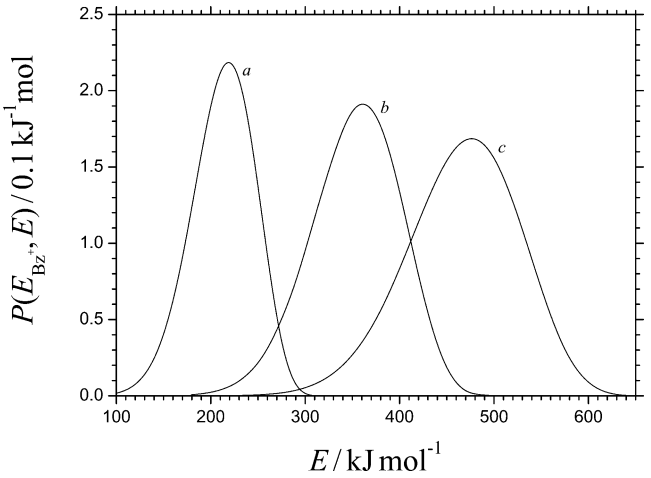

Figure 9. Energy distribution in Bz^+ arising from the primary $EtBz^+$ dissociation forming Bz^+ and CH_3 (statistical calculation with eq 20). (a) Initial energy E_{int} of $EtBz^+ = 323$ kJ mol^{-1}; (b) $E_{int} = 505$ kJ mol^{-1}; (c) $E_{int} = 658$ kJ mol^{-1}.

The energy partitioning between the vibrational energy of Bz^+ and CH_3 as well as their translational and rotational energy can be determined by statistical unimolecular rate theory. Because we are interested in only the internal energy distribution of Bz^+, we use the following simple approach: we identify those vibrations of $EtBz^+$ that correspond to Bz^+, and we split the $EtBz^+$ frequencies into the Bz^+ part and the rest. For a given total energy E, then, the statistical distribution of internal energy, $P(E_{Bz^+}, E)$, between the internal energy E_{Bz^+} of Bz^+ and the energy $E - E_{Bz^+}$ of the rest is given by

$$\mathrm{d}P(E_{Bz^+}, E) = \frac{\rho_{Bz^+}(E_{Bz^+})\, W_{\text{rest}}(E - E_{Bz^+})\, \mathrm{d}E_{Bz^+}}{W_{EtBz^+}(E)} \tag{20}$$

where $\rho(E)$ is the density of states, $W(E)$, is the number of states, and $P(E_{Bz^+}, E)$ is normalized to unity (i.e., $\int P(E_{Bz^+}, E)\, \mathrm{d}E_{Bz^+} = 1$). With the frequencies from Appendix A, distributions such as those shown in Figure 9 are obtained, which are very similar to those of corresponding systems.[11e,34]

In a manner analogous to that used in section 3.3, we calculate $k_{19}(E)$ by rigid activated complex RRKM theory using the B3LYP frequencies given in Appendix A and employing a threshold energy from the calculated minimum-energy path shown in Figure 10. At first we scale the B3LYP frequencies of Bz^+ by the same factor, 0.9, as used for $EtBz^+$ and use the unscaled B3LYP frequencies for structure L in Figure 10. The resulting $k_{19}(E)$ is shown as curve a in Figure 11. At the maximum energy of the Bz^+ energy distrubution in the N_2^+ and Ar^+ experiments, $k(E)$ has values on the order 10^5 to 10^6 s^{-1}. One would expect a much more substantial conversion of Bz^+ to Tr^+ unless a similarly fast quenching process of excited Bz^+ is present; with this value of $k_{19}(E)$, one would expect a much more substantial conversion of Bz^+ to Tr^+. The rate constant for the reverse of the reaction in eq 19, $k_{-19}(E)$, is calculated by the current method to be only about $^1/_3$ of $k_{19}(E)$. Because neither collisions nor secondary fragmentations under our conditions play a major role, quenching can occur only by radiative cooling (i.e., emission of infrared photons from the excited state). However, this process is known to take place on a 10^2- to 10^3-s^{-1} scale.[35−37] We therefore conclude that the simple DFT/RRKM calculation of $k_{19}(E)$, like that for $k_{13}(E)$,

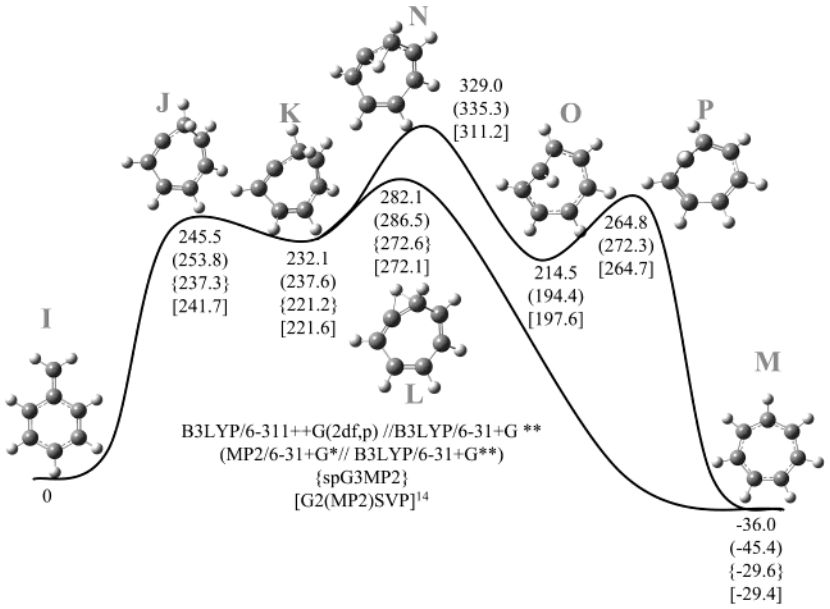

Figure 10. Calculated potential energy profiles for the isomerization of the benzylium cation to the tropylium cation; see the text.

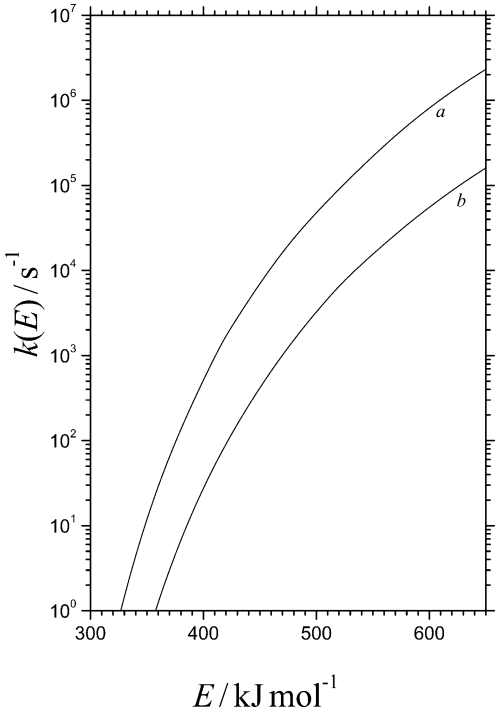

Figure 11. Specific rate constant for $Bz^+ \rightarrow Tr^+$ isomerization. (a) Modeling with unscaled transition-state frequencies from B3LYP calculations; (b) modeling with scaled transition-state frequencies; see the text for details.

gives values that are much too large. Because the radiative cooling rate is not known, the present results do not allow us to arrive at more quantitative conclusions. However, one may try to correct the B3LYP/RRKM results for $k_{19}(E)$ by complete analogy to $k_{13}(E)$ by using the B3LYP frequencies of Bz^+ scaled by the factor 0.9, using frequencies of transition state L scaled by the factor 1.09, and increasing the threshold energy of 282.1 kJ mol^{-1} by a factor of 1.05 as before. The result of this method for calculating $k_{19}(E)$ is also shown in Figure 11 as curve b. This $k_{19}(E)$ can be represented by

$$k_{19}(E) = 5.76 \times 10^2\,\mathrm{s}^{-1}\left[\frac{E - E_0}{157.9\ \mathrm{kJ\ mol}^{-1}}\right]^{7.076} \qquad (21)$$

with $E_0 = 297$ kJ mol^{-1}. As a result, only a small fraction of the high-energy part of the distribution from Figure 9 reaches up to energies where $k_{19}(E)$ exceeds 10^3 s^{-1} which in turn allows radiative cooling to be competitive. Although we cannot be entirely sure of this explanation for the unexpectedly small Tr^+ yields at high energies, in view of the modeling results for the dissociation of $EtBz^+$ to Tr^+ and CH_3 from section 3.3, this appears to be a plausible explanation.

4. Conclusions

Our observations of the energy dependence of the $[Tr^+]/([Tr^+] + [Bz^+])$ yield in the fragmentation of $EtBz^+$ can be well interpreted by a combination of rate measurements, electronic structure calculations, and RRKM rate calculations. The Tr^+ channel is characterized by a reverse barrier and a fairly rigid activated complex. Its transition-state frequencies appear to be higher than those derived from B3LYP calculations. Studies of secondary Tr^+ formation through the isomerization of Bz^+ to Tr^+ show that this process contributes at the highest excitation energies where isomerization becomes faster than radiative cooling of excited Bz^+ by IR emission. As with $EtBz^+$ fragmentation to $Tr^+ + CH_3$, electronic structure and RRKM rate calculations are consistent with observations only when transition-state frequencies are chosen that are higher than those derived from B3LYP calculations.

Acknowledgment. This work was funded by the Natural Sciences and Engineering Research Council of Canada, the Deutsche Forschungsgemeinschaft (SFB 357 "Molekulare Mechanismen unimolekularer Reaktionen"), and the United States Air Force Office of Scientific Research under project no. 2303EP4 and grant award no. F49620-03-1-0012. A.J.M. is supported through Visidyne contract number F19628-99-C-0069.

Appendix: Molecular Parameters Used in Modeling

1. Frequencies Used in Modeling (from B3LYP/6-31+G* Calculations, Unscaled, in cm^{-1}). *a. $C_8H_{10}^+$ (= $EtBz^+$):* 3240, 3232, 3223, 3213, 3206, 3146, 3128, 3058, 2955, 2951, 1666, 1537, 1508, 1505, 1479, 1434, 1411, 1402, 1388, 1363, 1291, 1236, 1227, 1196, 1161, 1096, 1057, 1045, 1020, 1012, 998, 993, 984, 957, 807, 803, 748, 679, 544, 537, 511, 407, 386, 353, 251, 213, 134, 43. For scaling factors used in modeling, see the text.

b. $C_7H_7^+$ *(=* Bz^+*):* 3264, 3232, 3230, 3213, 3211, 3207, 3163, 1668, 1600, 1577, 1503, 1481, 1427, 1387, 1355, 1214, 1204, 1136, 1106, 1047, 1024, 1018, 1001, 1000, 985, 849, 823, 797, 639, 627, 609, 534, 416, 360, 341, 164. For scaling factors used in modeling, see the text.

c. C_7H_7 *(=* Tr^+*):* 3209, 3204, 3204, 3195, 3195, 3186, 3186, 1634, 1633, 1566, 1565, 1516, 1516, 1439, 1311, 1311, 1253, 1253, 1076, 1076, 1059, 1059, 1013, 1013, 898, 898, 889, 889, 877, 662, 560, 558, 439, 439, 228, 223. For scaling factors used in modeling, see the text.

d. Transition-State Structure G (in Figure 7) for $C_8H_{10}^+$*(*$EtBz^+$*)* $\rightarrow$ $Tr^+ + CH_3$*:* 3299, 3291, 3211, 3206, 3202, 3195, 3191, 3184, 3184, 3114, 1639, 1607, 1552, 1552, 1505, 1505, 1433, 1423, 1421, 1307, 1304, 1255, 1232, 1062, 1057, 1047, 1026, 1009, 991, 920, 908, 899, 876, 873, 853, 693, 565, 556, 481, 459, 438, 429, 248, 240, 112, 95, 83. For scaling factors used in modeling, see the text.

e. Transition-State Structure C (in Figure 7) for $C_8H_{10}^+$*(*$EtBz^+$*)* $\rightarrow$ $C_8H_{10}^+$*(*$MeCHT^+$*):* 3228, 3225, 3213, 3211, 3207, 3202, 3119, 3067, 2982, 2789, 1634, 1572, 1487, 1480, 1474, 1466, 1417, 1397, 1357, 1284, 1217, 1201, 1157, 1123, 1100, 1060, 1046, 1045, 1021, 1018, 974, 970, 960, 927, 810, 795, 725, 616, 588, 528, 427, 386, 329, 302, 150, 75, 59. For scaling factors used in modeling, see the text.

f. Transition-State Structure L (in Figure 10) for $Bz^+ \rightarrow Tr^+$*:* 3220, 3217, 3203, 3189, 3180, 3140, 2130, 1829, 1619, 1568, 1446, 1408, 1370, 1324, 1258, 1239, 1215, 1093, 1048, 1032, 1015, 992, 942, 888, 869, 852, 807, 711, 687, 577, 506, 427, 377, 294, 284. For scaling factors used in modeling, see the text.

2. Energies Used in Modeling (from B3LYP/6-311++G(2df,p)//B3LYP/6-31+G Calculations, First Number Unscaled, Second Number Scaled by Fit to Experiments).** *a.* $C_8H_{10}^+ \rightarrow Tr^+ + CH_3$ *(Structure G in Figure 7):* 129.8 kJ mol^{-1} (unscaled), 136.7 kJ mol^{-1} (scaled).

b. $Bz^+ \rightarrow Tr^+$ *(Structure L in Figure 10):* 282.1 kJ mol^{-1} (unscaled), 297.0 kJ mol^{-1} (scaled).

References and Notes

(1) Dunbar, R. C. *J. Am. Chem. Soc.* **1975**, *97*, 1382.

(2) Shen, J.; Dunbar, R. C.; Olah, G. A. *J. Am. Chem. Soc.* **1974**, *96*, 6227.

(3) (a) Jackson, J. A.; Lias, S. G.; Ausloos, P. *J. Am. Chem. Soc.* **1977**, *99*, 7515. (b) Ausloos, P. *J. Am. Chem. Soc.* **1982**, *104*, 5259.

(4) Stapleton, B. J. Bowen, R. D.; Williams, D. H. *J. Chem. Soc., Perkin Trans. 2* **1979**, 1219.

(5) McLafferty, F. W.; Bockhoff, F. M. *J. Am. Chem. Soc.* **1979**, *101*, 1783.

(6) Grotemeyer, J.; Grützmacher, H.-F. *Org. Mass Spectrom.* **1982**, *17*, 353.

(7) Bombach, R.; Dannacher, J.; Stadelmann, J. P. *Chem. Phys. Lett.* **1983**, *95*, 259.

(8) Buschek, J. M.; Ridal, J. J.; Holmes, J. L. *Org. Mass Spectrom.* **1988**, *23*, 543.

(9) Lifshitz, C.; Gotkis, Y.; Ioffe, A.; Laskin, J.; Shaik, S. *Int. J. Mass Spectrom. Ion Processes* **1993**, *125*, R7.

(10) (a) Oh, S. T.; Choe, J. C.; Kim, M. S. *J. Phys. Chem.* **1996**, *100*, 13367. (b) Hwang, W. G.; Moon, J. H.; Choe, J. C.; Kim, M. S. *J. Phys. Chem. A* **1998**, *102*, 7512. (c) Moon, J. H.; Choe, J. C.; Kim, M. S. *J. Phys. Chem. A* **2000**, *104*, 458. (d) Kim, Y. H.; Choe, C. J.; Kim, M. S. *J. Phys. Chem. A* **2001**, *105*, 5751.

(11) (a) Arnold, S. T.; Dotan, I. Williams, S.; Viggiano, A. A.; Morris, R. A. *J. Phys. Chem. A* **2000**, *104*, 928. (b) Williams, S.; Midey, A. J.; Arnold, S. T.; Morris, R. A.; Viggiano, A. A.; Chiu, Y. H.; Levandier, D. J.; Dressler, R. A. *J. Phys. Chem. A* **2000**, *104*, 10336. (c) Midey, A. J.; Williams, S.; Arnold, S. T.; Viggiano, A. A. *J. Phys. Chem. A* **2002**, *106*, 11726. (d) Viggiano, A. A.; Miller, T. M.; Williams, S.; Arnold, S. T.; Seeley, J. V.; Friedman, J. F. *J. Phys. Chem. A* **2002**, *106*, 11917. (e) Troe, J.; Viggiano, A. A.; Williams, S. *J. Phys. Chem. A* **2004**, *108*, 1574.

(12) (a) Cone, C.; Dewar, J. S.; Landman, D. *J. Am. Chem. Soc.* **1977**, *99*, 372. (b) Dewar, M. J. S.; Landman, D. *J. Am. Chem. Soc.* **1977**, *99*, 2446.

(13) (a) Athanassios, N.; Radom, L. *J. Am. Chem. Soc.* **1994**, *116*, 9760. (b) Athanassios, N.; Radom, L. *J. Am. Chem. Soc.* **1997**, *119*, 11933.

(14) Smith, B. J.; Hall, N. E. *Chem. Phys. Lett.* **1997**, *279*, 165.

(15) Reindl, B.; Clark, T.; Schleyer, P. v. R. *J. Phys. Chem. A* **1998**, *102*, 8953.

(16) Shin, C.-H.; Park, K.-C.; Kim, S.-J.; Kim, B. *Bull. Korean Chem. Soc.* **2002**, *23*, 337.

(17) Lifshitz, C. *Acc. Chem. Res.* **1994**, *27*, 138.

(18) Ausloos, P.; Jackson, J.-A. A.; Lias, S. G. *Int. J. Mass Spectrom. Ion Phys.* **1980**, *33*, 269.

(19) Malow, M.; Penno, M.; Weitzel, K.-M. *J. Phys. Chem. A* **2003**, *107*, 10625.

(20) Su, T.; Chesnavich, W. J. *J. Chem. Phys.* **1982**, *76*, 5183.

(21) Viggiano, A. A.; Morris, R. A.; Dale, F.; Paulson, J. F.; Giles, K.; Smith, D.; Su, T. *J. Chem. Phys.* **1990**, *93*, 1149.

(22) Ikezoe, Y.; Matsuoka, S.; Takebe, M.; Viggiano, A. A. *Gas-Phase Ion−Molecule Reaction Rate Constants Through 1986*; Maruzen Company, Ltd.: Tokyo, 1987.

(23) Ferguson, E. E. *J. Phys. Chem.* **1986**, *90*, 731.

(24) Curtiss, L. A.; Redfern, P. C.; Raghavachari, K.; Rassolov, V.; Pople, J. A. *J. Chem. Phys.* **1999**, *110*, 4703.

(25) Frisch, M. J.; Trucks, G. W.; Schlegel, H. B.; Scuseria, G. E.; Robb, M. A.; Cheeseman, J. R.; Zakrzewski, V. G.; Montgomery, J. A., Jr.; Stratmann, R. E.; Burant, J. C.; Dapprich, S.; Millam, J. M.; Daniels, A. D.; Kudin, K. N.; Strain, M. C.; Farkas, O.; Tomasi, J.; Barone, V.; Cossi, M.; Cammi, R.; Mennucci, B.; Pomelli, C.; Adamo, C.; Clifford, S.; Ochterski, J.; Petersson, G. A.; Ayala, P. Y.; Cui, Q.; Morokuma, K.; Malick, D. K.; Rabuck, A. D.; Raghavachari, K.; Foresman, J. B.; Cioslowski, J.; Ortiz, J. V.; Stefanov, B. B.; Liu, G.; Liashenko, A.; Piskorz, P.; Komaromi, I.; Gomperts, R.; Martin, R. L.; Fox, D. J.; Keith, T.; Al-Laham, M. A.; Peng, C. Y.; Nanayakkara, A.; Gonzalez, C.; Challacombe, M.; Gill, P. M. W.; Johnson, B. G.; Chen, W.; Wong, M. W.; Andres, J. L.; Head-Gordon, M.; Replogle, E. S.; Pople, J. A. *Gaussian 98*, revision A.7; Gaussian, Inc.: Pittsburgh, PA, 1998.

(26) Troe, J.; Ushakov, V. G.; Viggiano, A. A.; Wiliams, S. To be submitted for publication.

(27) Lias, S. G.; Bartmess, J. E.; Liebman, J. F.; Holmes, J. L.; Levin, R. D.; Mallard, W. G. *J. Phys. Chem. Ref. Data* **1988**, *17*, Suppl 1.

(28) Actually, he says that the estimation of the relative abundance of the two isomers "*may tend to underestimate the reactive* (Bz^+) *isomer somewhat, since a small fraction of these ions may react at short times*...,". See ref 3b.

(29) Lias, S. G.; Bartmess, J. E.; Holmes, J. L.; Levine, R. D.; Mallard, W. G. *J. Phys. Chem. Ref. Data* **1988**, Suppl 1.

(30) Schroeder, J.; Steinel, T.; Troe, J. *J. Phys. Chem. A* **2002**, *106*, 5510.

(31) Foresman, J. B.; Frisch, A. E. *Exploring Chemistry with Electronic Structure Methods*, 2nd ed.; Gaussian, Inc.: Pittsburgh, PA, 1996.

(32) Pople, J. A.; Scott, A. P.; Wong, M. W. Radom, L. *Isr. J. Chem.* **1993**, *33*, 345.

(33) Troe, J. *J. Phys. Chem.* **1983**, *87*, 1800.

(34) Baer, T.; Hase, W. L. *Unimolecular Reaction Dynamics: Theory and Experiments*; Oxford University Press: New York, 1996; pp 332.

(35) Shi, J.; Berfeld, D.; Barker, J. R. *J. Chem. Phys.* **1988**, *88*, 6211.

(36) Barker, J. R. *J. Phys. Chem.* **1992**, *96*, 7361.

(37) Dunbar, R. C. *J. Phys. Chem.* **1994**, *98*, 8705.